Inelastic Scattering of He Atoms and NO($X^2\Pi$) Molecules: The Role of Parity on the Differential Cross Section[†]

F. J. Aoiz and J. E. Verdasco

Departamento de Química Física, Facultad de Química, Universidad Complutense, 28040 Madrid, Spain

M. Brouard*

The Department of Chemistry, The Physical and Theoretical Chemistry Laboratory, South Parks Road, Oxford, OX1 3QZ, United Kingdom

J. Kłos

Departamento de Química Física, Facultad de Química, Universidad Complutense, 28040 Madrid, Spain, and Department of Chemistry and Biochemistry, University of Maryland, College Park, Maryland 20472

S. Marinakis

LPMAA, CNRS UMR 7092, Université Pierre et Marie Curie (Paris 6), 3 rue Galilée, 94200 Ivry sur Seine, France

S. Stolte

Laser Center and Department of Physical Chemistry, Vrije Universiteit Amsterdam, De Boelelaan 1083, 1081 HV Amsterdam, The Netherlands, and Atomic and Molecular Physics Institute, Jilin University, Changchun 130012, China

Received: May 11, 2009; Revised Manuscript Received: June 30, 2009

Quasiclassical trajectory (QCT) and quantum mechanical (QM) close-coupling calculations have been used to study the state-resolved rotationally inelastic scattering of NO($X^2\Pi_{1/2}$,$v = 0$,$j = 1/2$,e/f) by He on the most recent ab initio potential energy surface of J. Kłos et al. [*J. Chem. Phys.* **2000**, *112*, 2195.]. Opacity functions, and integral and differential cross sections are reported at collision energies of 63 and 147 meV and compared with previous theoretical calculations and experimental measurements on this and other systems. The existence of double peaks in the QCT and QM differential cross sections is examined in detail. While at a collision energy of 147 meV two rotational peaks appear in both the QCT and open-shell QM results, only a single peak is found in the QM calculations at the lower collision energy. The double peaks in the quantum-state-resolved differential cross sections (DCS) are found to be closely related to structure found in the corresponding state-resolved opacity functions. The structure in the QCT and QM DCSs is attributed to a flattening of the potential energy surface for sideways approach of He to the near-symmetric NO(X) molecule, and in both sets of calculations, it is shown to arise from a specific odd term in the expansion of the intermolecular potential. Although significant differences are found between the QCT and QM data in the forward scattered direction, and for higher final rotational levels, reflecting differences in the nature of the rotational rainbows observed in these two methods, in general, the QCT calculations are shown to give similar results to quantum theory. Furthermore, they provide valuable clues as to the mechanism of rotational energy transfer in this system.

I. Introduction

The transfer of energy and momentum by inelastic collisions is central to understanding chemical processes. Both experimental and theoretical studies have provided detailed information on inelastic scattering involving closed-shell molecules.[1,2] However, processes involving open-shell species, which underlie much of chemical kinetics, are more involved due to the possibility of transitions between different spin−orbit and/or Λ-doublet states and, as such, are attracting growing interest.[3,4] Collisions between noble gas atoms and diatomic molecules are prototypes for such encounters.[5−9] In particular, collisions between the rare gases and NO(X) have emerged as paradigms for studying multisurface collisions of open-shell molecules, with work dating back more than 20 years. This is largely due to the fact that the NO(X) molecule, while theoretically challenging, is a stable radical that can be easily detected using techniques such as resonantly enhanced multiphoton ionization (REMPI) or laser-induced fluorescence (LIF).

The ground state of the NO radical has a $1\sigma^2 2\sigma^2 3\sigma^2 4\sigma^2 1\pi^4 5\sigma^2 2\pi^1$ electronic configuration, which gives rise to a $^2\Pi$ term. In Hund's case (a), which is valid for the lowest rotational states of NO(X), the projection of the electronic orbital angular momentum, ***L***, on the internuclear axis, $\Lambda = \pm 1$, and the projection of the electron spin momentum, ***S***, on the

---

[†] Part of the "Vincenzo Aquilanti Festschrift".

* To whom correspondence should be addressed. E-mail: mark.brouard@chem.ox.ac.uk.

10.1021/jp9043732

internuclear axis, $\Sigma = \pm 1/2$, couple together. This coupling results in two spin−orbit states, a low-lying $^2\Pi_{1/2}$ state with $\Omega \equiv |\Lambda + \Sigma| = 1/2$ and a higher-energy $^2\Pi_{3/2}$ state with $\Omega = 3/2$ (we use the notation Ω to denote $|\Omega|$). The rotational manifolds that arise from the $^2\Pi_{1/2}$ and $^2\Pi_{3/2}$ states are termed F_1 and F_2, respectively. For the F_2 manifold, the lowest rotational level has $j = 1.5$, and for the F_1 manifold, the lowest rotational level has $j = 0.5$, where j is the quantum number for the total angular momentum excluding nuclear spin. Because of the interaction between the electronic orbital and rotational angular momenta, each rotational level is split into two Λ-doublet components. Considering the space-fixed inversion operator E^*, $E^*\psi = \pm\psi$, if a NO molecule in a specific quantum state transforms according to the upper sign, the state has a positive parity, $p = +1$, and if it transforms according to the lower sign, the state has a negative parity, $p = -1$. This parity is related to the symmetry index or spectroscopic parity index, ϵ, by $\epsilon = p(-1)^{j-1/2}$. Λ-doublet components with $\epsilon = +1$ are designated by the label e and the $\epsilon = -1$ levels by the label f. The f levels are slightly higher in energy than the e. In addition to the labels e and f, the NO(X) Λ-doublet levels are usually labeled as A′ or A″, depending on whether the electronic wave function is symmetric or antisymmetric with respect to reflection in the plane of rotation. In the high j limit, the unpaired electron lies in the plane of rotation in the A′ states and lies perpendicular to that plane in the A″ states.[10] The F_1e and F_2f Λ-doublet components are designated with the label A′, and the F_1f and F_2e are designated with A″.

Numerous studies have been reported on the He−NO(X) system. Using crossed supersonic molecular beam techniques,[11,12] coupled with either LIF[13] or REMPI[14] spectroscopy, relative values of the integral and differential cross sections for transfer of translational energy to specific rotationally or electronically excited quantum states have been obtained. The same method has been used to obtain integral cross sections (ICS) for collisions of vibrationally excited NO($X^2\Pi_{1/2}, v = 20, j = 0.5$,e/f).[15] Westley et al. combined crossed molecular beams with imaging techniques to obtain angular distributions at a mean collision energy of 60.9 meV (491 cm^{-1}).[16] Using a rotatable molecular beam source, Barrass et al. obtained ICSs at collision energies in the range of 32−120 meV.[17] Unfortunately, with experiments of this type, absolute values of the cross sections cannot be determined. Furthermore, the initial states in these experiments are restricted to the lowest rotational levels populated by jet cooling, and preparation of specific Λ-doublet states is not feasible because the two states lie too close in energy. Optical−optical double resonance techniques[18,19] have the particular advantage that absolute rate coefficients for total relaxation from a selected initial level as well as state-to-state rate coefficients can be obtained.[20,21] More recently, using hexapole focusing techniques, it has proved possible to select the initial Λ-doublet component of the lowest rotational level of NO(X).[22] Stolte and co-workers recently presented an ion-imaging study in which differential cross sections (DCS) for collisions between fully state-selected NO($X, v = 0, j = 1/2, \Omega = 1/2$,f) molecules with He atoms[23] were determined for the first time. They have subsequently used a quasiquantum treatment (QQT) to rationalize interesting propensities observed in the DCSs for this system.[24−28]

There has also been a considerable amount of previous theoretical work on the He−NO(X) system. Coupled states and infinite-order sudden calculations of the ICSs at a range of collision energies have been carried out by Corey and Alexander,[29] for both multiplet-preserving and -changing transitions, employing an Ar−NO(X) potential energy surface (PES) of Nielson et al.[30] but using a reduced mass appropriate to collisions with He. The first ab initio PESs were obtained within the coupled electron pair approximation (CEPA) and have been used by Yang and Alexander for close-coupling and coupled state calculations, performed using the HIBRIDON package,[31−33] to provide state-to-state ICSs at collision energies of 63, 147, and 300 meV and DCSs at 147 meV.[34] Close-coupled quantum scattering calculations have also been carried out to simulate the experiments employing vibrationally excited NO molecules,[15] and ICSs were reported at a collision energy of 24.2 meV. The cross sections exhibited intense Δj = even (odd) propensity for the e/f symmetry-conserving (changing) spin−orbit-preserving collisions. In a subsequent study,[35] Alexander obtained degeneracy-averaged DCSs and differential angular momentum alignments for $j' = 4.5$, 6.5, and 12.5 for both multiplet-preserving and multiplet-changing collisions using a collision energy of 147 meV. Westley et al.[16] also used the PES of Yang and Alexander[34] to obtain DCSs for transitions both within and between the two spin−orbit manifolds at a collision energy of 60.9 meV. Although more accurate adiabatic potential energy surfaces for the He−NO(X) system have been available for some time,[36] these PESs have not been used in dynamical calculations until quite recently.[9,23,37−39]

The aim of the present study is to employ the latest, high-quality ab initio PESs obtained by Kłos et al.[36] for both quasiclassical trajectory (QCT) and quantum mechanical (QM) calculations. A preliminary Communication of some aspects of these calculations has been presented previously.[37] We focus exclusively on collisions of NO($X^2\Pi_{1/2}, v = 0, j = 1/2$,e/f). Detailed comparisons between experiment and theory are presented, and the strengths and weaknesses of the QCT method in inelastic scattering assessed. The outline of the paper is as follows. In section II, previous work on PESs and scattering calculations on them are briefly reviewed, followed by computational details of the QCT and QM methodologies employed in the present work. Then, in section III, the results are presented and discussed in the following order: integral cross sections, opacity functions, and differential cross sections. Finally, continuing our previous work on He−NO(X),[37] we examine the role of specific expansion terms in the PESs. We summarize the main conclusions of the paper in section IV.

II. Calculations

A. He−NO(X) PESs. Two potential surfaces are required to describe collisions between NO($^2\Pi_{1/2}$) molecules with He atoms of ^{2}A′ and ^{2}A″ symmetry. In the A′ state (from now on, we drop the superscript doublet notation for simplicity), the singly occupied π^* orbital of NO(X) is located in the N−O−He plane, while in the second, it lies perpendicular to it. The diabatic potentials employed in both the QCT and the QM calculations were constructed from the adiabatic A′ and A″ RCCSD(T) PESs mentioned above.[36] Alexander has shown[5] that for Hund's case (a) molecules, the multiplet-preserving transitions

$$\mathrm{NO}(^2\Pi_{1/2}, j = 0.5, \mathrm{e/f}) + \mathrm{He} \rightarrow \mathrm{NO}(^2\Pi_{1/2}, j', \mathrm{e/f}) + \mathrm{He} \tag{1}$$

occur on the average potential

$$V_{\mathrm{sum}}(R, \gamma) = \frac{V_{\mathrm{A''}}(R, \gamma) + V_{\mathrm{A'}}(R, \gamma)}{2} \tag{2}$$

whereas the multiplet-changing transitions

$$\mathrm{NO}(^2\Pi_{1/2}, j = 0.5, \mathrm{e/f}) + \mathrm{He} \rightarrow \mathrm{NO}(^2\Pi_{3/2}, j', \mathrm{e/f}) + \mathrm{He} \tag{3}$$

are coupled by the difference potential

$$V_{\mathrm{diff}}(R, \gamma) = \frac{V_{\mathrm{A}''}(R, \gamma) - V_{\mathrm{A}'}(R, \gamma)}{2} \tag{4}$$

In eqs 2 and 4, R is the distance between the He atom and the center of mass of the NO(X) molecule, and γ is the Jacobi angle that describes the initial orientation of the diatomic axis with respect to the vector $\boldsymbol{R}$. In this work, $\gamma < 90°$ refers to He atom approach towards the N-end of the molecule; that is, $\gamma = 0°$ for the linear He−N−O configuration. The potential is calculated with the NO(X) bond length set to its equilibrium value, $r_e = 1.15077$ Å.[40]

The sum and difference potentials, $V_{\mathrm{sum}}(R,\gamma)$ and $V_{\mathrm{diff}}(R,\gamma)$, are plotted in Figure 1. As will become apparent, a particularly important feature of the summed potential is the flattening at approach angles of around 90°. The difference potential is significantly smaller at large $\boldsymbol{R}$ values than the summed potential and is negative for most approach geometries. The reason for this has been discussed in detail previously by Dagdigian and co-workers[41] and is associated with the fact that for a molecule with a π^1 configuration, the A′ state tends to be more repulsive since the unpaired electron lies in the triatomic plane.

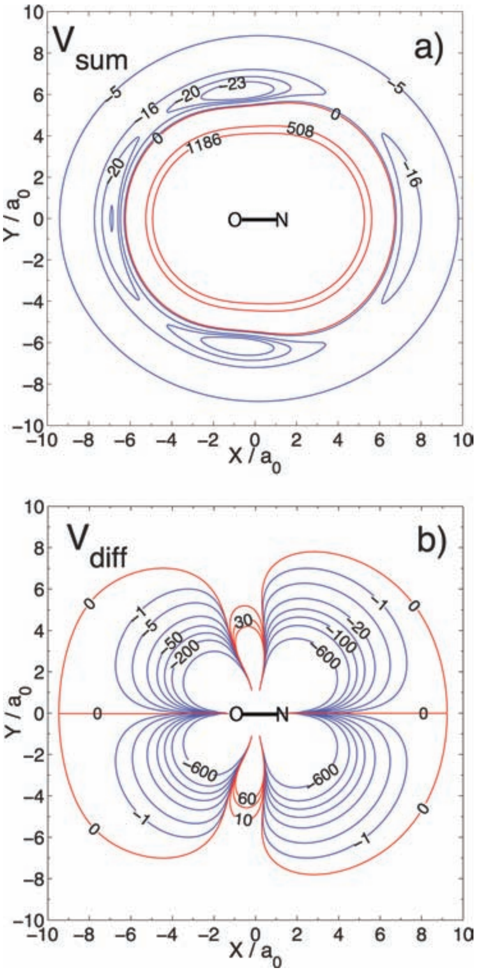

Figure 1. Contour plots of the RCCSD(T) (a) sum (V_{sum} of eq 2) and (b) difference (V_{diff} of eq 4) potentials for He + NO(X).[36] The O-end of the diatomic is on the left side of the figure. The units are in bohr for both axes. The contour lines in red represent zero and positive potential energy. Contours are in cm^{-1}, with the two inner contours corresponding to 63 (508 cm^{-1}) and 147 meV (1186 cm^{-1}), respectively, the collision energies of the present study. Note the slight flattening of the sum potential for T-shaped configurations.

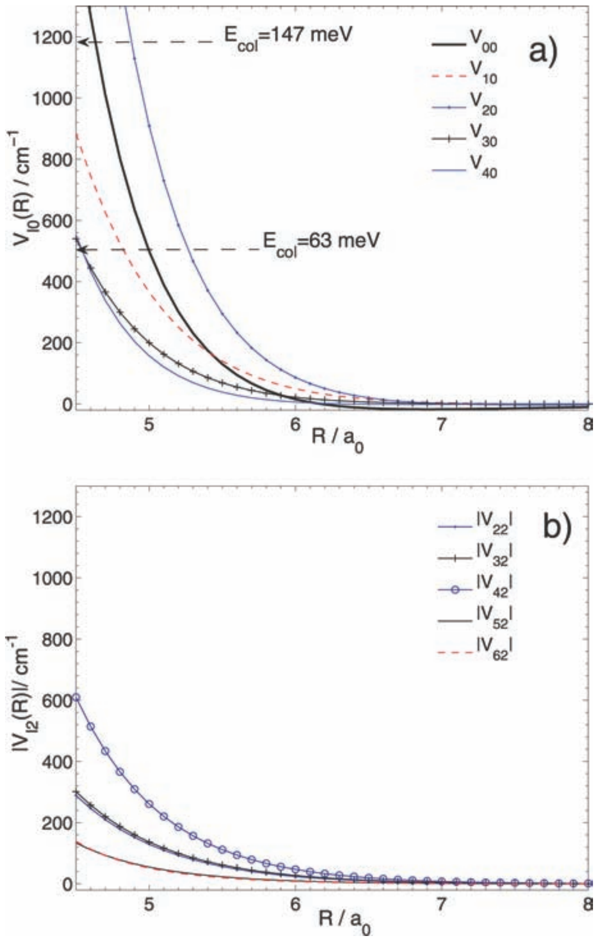

Figure 2. Plots of the radial dependence of the expansion coefficients for the RCCSD(T) (a) sum ($V_{l0}(R)$ of eq 5) and (b) difference (V_{l2} of eq 6) potentials for He + NO(X).[36] Note that the moduli of the expansion terms in the difference potential are shown, $|V_{l2}|$; all of those shown are negative.

It is convenient, particularly for the QM scattering calculations, to expand $V_{\mathrm{sum}}(R,\gamma)$ and $V_{\mathrm{diff}}(R,\gamma)$ in series using the reduced rotation matrix elements

$$V_{\mathrm{sum}}(R, \gamma) = \sum_{l=0}^{\infty} V_{l0}(R) d^{l}_{00}(\gamma) \tag{5}$$

and

$$V_{\mathrm{diff}}(R, \gamma) = \sum_{l=2}^{\infty} V_{l2}(R) d^{l}_{20}(\gamma) \tag{6}$$

The coefficients of the expansions, $V_{l0}(R)$ and $V_{l2}(R)$, are shown in Figure 2. Note that $V_{\mathrm{sum}}(R,\gamma)$ is dominated by low-order even terms, V_{00} and V_{20}, and that V_{30} is considerably smaller than V_{10}. V_{00} only contributes to elastic scattering. For the difference potential, all of the coefficients are negative and, as noted above, have a considerably shorter range than those of the sum potential at the energies of the present experiments.

B. Computational Methods. ***1. QCT Calculations.*** The quasiclassical trajectory (QCT) method employed here is similar to that used in a recent study of inelastic scattering of NO(X) by Ar,[42] and only specific details important to this study are presented here. The reader is directed elsewhere for a more detailed description of the QCT method.[43,44]

Batches of 10^6 trajectories were run at each of the collision energies, 508 and 1186 cm^{-1} (63 and 147 meV, respectively), with the NO(X) molecule initially in its lowest rotational state. Because the potential energy is calculated with the NO(X) bond length set to its equilibrium value, the integration of the classical equations of motion was accomplished using the method of Lagrange multipliers to constrain r to r_e. The Hammings fourth-order predictor, fourth-order corrector algorithm with a fixed time step size was employed for the numerical integration of the equations of motion. The integration step size used here was 5×10^{-17} s, which resulted in a conservation of the total energy better than 1 part in 10^5 and better than 1 part in 10^7 in the total angular momentum.

Assignment of the final rotational quantum number j' was made by equating the square of the classical angular momentum $|\mathbf{j}'|^2$ with $j'(j' + 1)/\hbar^2$ and rounding to the nearest integer. In the case of $j' = 1$, only trajectories leading to j' in the range of 1.0−1.5 were taken into account. This criterion was also employed in a previous study[42] and appears justified based on comparison with both experimental and QM results. Although it may lead to an underestimation of the $\Delta j = j' - j = 1$ cross section, it provides a safeguard that only inelastic collisions are taken into account for that transition. If trajectories with j' in the interval [0.5, 1.0] were also taken into account, the QCT cross sections for $\Delta j = 1$ would be increased roughly by a factor of about 2. The value of the maximum impact parameter, $b_{\max}$, was chosen such that there were no inelastic trajectories ($\Delta j >$ 0.5) even for impact parameters slightly smaller than $b_{\max}$. With this procedure, values of 3.6 and 3.5 Å were derived for $b_{\max}$ at E_{coll} of 63 and 147 meV, respectively. The opacity functions and DCSs were calculated by the method of moment expansion in Legendre polynomials.[44]

2. QM Calculations. The finite set of coupled equations[45] was solved numerically with increasing total angular momentum quantum number, J, until the desired cross sections converged. Two kinds of quantum close-coupling (CC) calculations were performed. The first calculations were performed using the nonadiabatic approach with two diabatic potentials for He−NO(X) (V_{sum} and V_{diff}) and took into account the electronic structure of the open-shell molecule. The open-shell calculations assumed the molecule to be initially in either e or f states of NO($X^2\Pi_{1/2}, v = 0, j = 1/2$). The second kind of CC calculations were performed only on the V_{sum} potential, treating NO(X) as a closed-shell diatomic. The results from these two sets of calculations will be denoted hereafter as o-s QM and c-s QM, respectively, and will be compared with the predictions from the (closed-shell) QCT calculations. For the o-s QM calculations, the HIBRIDON suite of codes,[33] which uses the log-derivative propagator by Manolopoulos and Alexander,[31,32,46] was employed. For the c-s QM case, both the HIBRIDON and the MOLSCAT package[47] were used, although both codes gave essentially the same results. The close-coupling calculations at $E_{\text{coll}} = 63$ meV employed all partial waves with total angular momentum quantum number up to $J = 101.5$ and NO final rotational levels up to $j' = 13.5$. For the collision energy of 147 meV, partial waves with J up to 200.5 and NO(X) final rotational levels up to $j' = 25.5$ were included.

In the closed-shell calculations (QCT and QM), we treat the NO molecule as a rigid rotor with no internal (electronic orbital or spin) angular momenta. We have assumed here that QCT or c-s QM cross sections from transitions from the lowest rotational level $j = 0$ to the level $j' = j + \Delta j$ can be compared directly with transitions from the $j = 1/2$, $\Omega = 1/2$ to the level $j' = 1/2 + \Delta j$, summing the contributions of $\Delta\Omega = 0$ and 1. In addition, since the o-s QM transition for each Δj corresponds to four distinct Λ-doublet-resolved transitions (e → e, e → f, f → e, and f → f), we have assumed that the QCT or c-s QM cross sections, $\sigma(\Delta j)$, should be compared with the average over the two initial Λ-doublet levels and the sum over the two final Λ-doublet levels, that is

$$\sigma^{\text{c-s QM}}(\Delta j) \leftrightarrow \frac{1}{2} \sum_{\Omega'} \sum_{\epsilon,\epsilon'} \sigma^{\text{o-s QM}}(\Omega, j, \epsilon \rightarrow \Omega', j', \epsilon') \tag{7}$$

Unless stated to the contrary, we will use this equivalence.

Before presenting and discussing the results of the calculations, it is helpful to recall the propensities that might be expected based on consideration of the potential matrix elements alone.[5,41,48] As stated in the Introduction, the initial and final state Λ-doublet levels are labeled by parity indices ϵ and ϵ', which take values of +1 or −1 for e and f levels, respectively. The potential matrix elements in the Hund case (a) limit (valid in the limit of low j) are given by[5,41,48]

$$\begin{aligned}\langle j'L'\Omega'\epsilon'JM|V|jL\Omega\epsilon JM\rangle = \\ (-1)^{j+j'+J-\Omega}([j][j'][L][L'])^{1/2} \sum_l \begin{pmatrix} L' & l & L \\ 0 & 0 & 0 \end{pmatrix} \begin{Bmatrix} j & L & J \\ L' & j' & l \end{Bmatrix} \times \\ F_l(j\epsilon, j'\epsilon') G_l(j\Omega\epsilon, j'\Omega'\epsilon')\end{aligned} \tag{8}$$

where we use the notation $[n] = (2n + 1)$, L is the orbital angular momentum quantum number, and (:::) and {:::} are 3j and 6j symbols,[49] respectively. The terms F_l and G_l are given by

$$F_l(j\epsilon, j'\epsilon') = \frac{1}{2}[1 - \epsilon\epsilon'(-1)^{j+j'+l}] \tag{9}$$

and

$$\begin{aligned}G_l(j\Omega\epsilon, j'\Omega'\epsilon') = \delta_{\Omega\Omega'} V_{l0}(R) \begin{pmatrix} j' & l & j \\ -\Omega & 0 & \Omega \end{pmatrix} - \\ \epsilon(1 - \delta_{\Omega\Omega'}) V_{l2}(R) \begin{pmatrix} j' & l & j \\ -\Omega' & 2 & -\Omega \end{pmatrix}\end{aligned}$$

respectively. The l is a non-negative integer number used in the expansion of the γ dependence of the sum and difference potentials, as defined in eqs 5 and 6. Note that for half-integers j and j', the $(-1)^{j+j'+l}$ term in the symmetry factor, F_l, may be written as $-(-1)^{\Delta j+l}$. In the intermediate coupling case, eq 8 remains valid, with Ω and Ω' replaced by the corresponding F_1 or F_2 states, and the definition of the potential term $G_l(\cdots)$ changed to allow for the mixing of the spin−orbit states.[41] Orlikowski and Alexander have shown that, because of the F_l term in eq 8, potential terms with l = even couple Δj = even transitions for $\epsilon' = \epsilon$ and Δj = odd transitions for $\epsilon' \neq \epsilon$, while

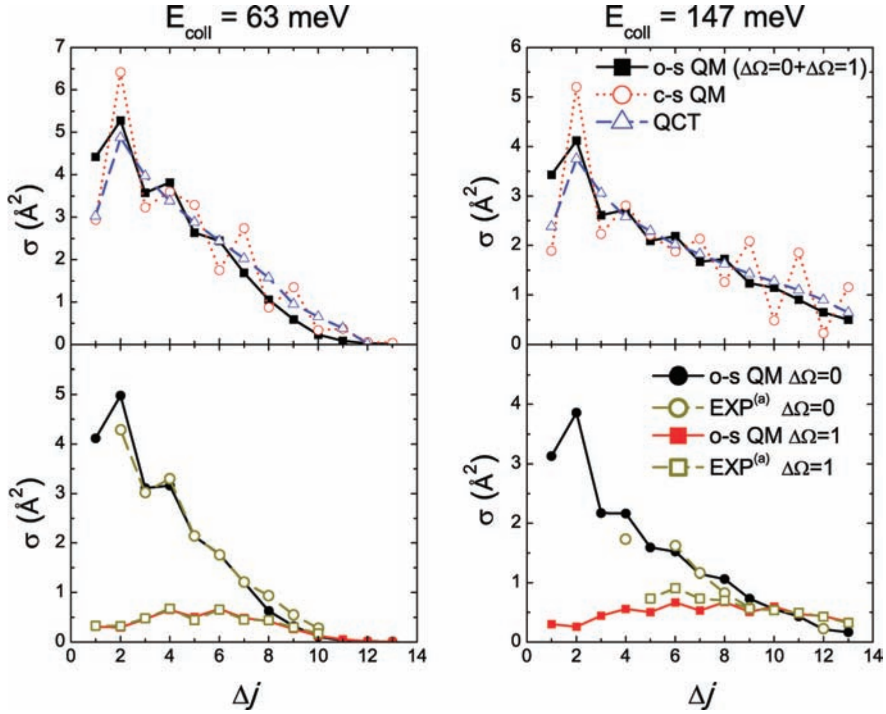

Figure 3. Upper panels: Comparison between QCT (blue Δ) and o-s QM (black ■) and c-s QM (red ○) rotationally resolved ICSs for the scattering of He by NO(X) at $E_{coll} = 63$ (upper left panel) and 147 meV (upper right panel). The o-s QM ICSs are summed over spin−orbit transitions. Lower panels: Comparison of the o-s QM results for $F_1 \rightarrow F_1$ (black ●) and $F_1 \rightarrow F_2$ (red ■) spin−orbit-changing ICSs with the experimental measurements by Joswig et al.[13] at 63 meV (bottom left panel) and Meyer[14] at 147 meV (bottom right panel). The experimental data are shown with open symbols. The o-s QM ICSs in each of the four panels have been summed over final and averaged over initial Λ-doublet components, and the initial state is NO($^2\Pi_{1/2}$,$v = 0$,$j = 0.5$).

potential terms with l = odd couple Δj = odd transitions for $\epsilon' = \epsilon$ and Δj = even transitions for $\epsilon' \neq \epsilon$.[48] Therefore, if even terms in the expansion of the angular part of the potential dominate, there will be a propensity for even Δj transitions for $\epsilon' = \epsilon$ and a propensity for odd Δj transitions otherwise.

III. Results and Discussion

A. Integral Cross Sections. The upper panels of Figure 3 compare the j' dependence of the ICSs obtained from the QCT, c-s QM, and o-s QM calculations at 63 and 147 meV. As indicated above, the o-s QM calculations have been summed over both $F_1 \rightarrow F_1$ and $F_1 \rightarrow F_2$ transitions and final Λ-doublet states and have been averaged over the initial Λ-doublet states. The QCT results generally lie close to the c-s QM and o-s QM calculations. Note that the c-s QM calculations tend to show somewhat more pronounced oscillatory structure than the state averaged o-s QM data (see further below). The ICS results from the present theoretical work are in very good agreement with the previous QM calculations by Yang and Alexander, not presented in Figure 3 for reasons of clarity, employing their ab initio PESs.[34]

The lower panels of Figure 3 compare the calculated ICSs, resolved into spin−orbit-conserving and -changing collisions, with the experimental data of Joswig et al.[13] at a collision energy of 63 meV and that of Meyer[14] at 147 meV. Because the experimental measurements provided only relative values for the cross sections, they have been scaled so that their sum is equal to that of the o-s QM calculations averaged over initial and summed over final Λ-doublet transitions. Using this scaling scheme, the experimental results are found to be in good agreement with the theoretical calculations, although the agreement is somewhat better at the lower collision energy. At low Δj, the ICSs for the spin−orbit-changing transitions are much smaller than those for their spin−orbit-conserving counterparts. This most likely reflects differences in V_{sum} and V_{diff}. The latter is generally weaker than the average potential (see Figures 1 and 2), and for low Δj, for which Hund's case (a) is a good description of both the initial and final NO(X) rotational state, it is therefore not surprising that the difference potential is unable to induce significant spin−orbit-changing collisions. For higher Δj, NO(X) belongs more to an intermediate coupling case, and both the average and the difference potentials contribute to multiplet-conserving and -changing transitions, and such a big difference in ICS is not expected.[41] The lower panels of Figure 3 show that for high final rotational levels (populated by $\Delta j \gtrsim 8$), the spin−orbit-changing transitions have similar cross sections to the spin−orbit-conserving ones.

Figure 4 shows the o-s QM ICSs at $E_{coll} = 147$ meV for the spin−orbit-conserving (panel a) and -changing (panel b) collisions, resolved into Λ-doublet levels. Note that in the limit of Hund's case (a), the values of the ICSs for e → e and e → f transitions should be identical to those for f → f and f → e, respectively.[41] However, for the spin−orbit state-conserving transitions, the ICSs for the e → f are slightly higher than those for the f → e transitions, and the f → f cross sections are slightly higher than those for the corresponding e → e cross sections. The reverse is true for the spin−orbit-changing collisions. Similar propensities were observed at $E_{coll} = 63$ meV, confirming the previous work of refs 9 and 15. Dagdigian et al.[41] have explained this type of propensity for molecules of both π^1 and π^3 electronic occupancy. As mentioned above, they noted that for a molecule with π^1 configuration, the A′ potential surface is more repulsive than the A″ surface. Because of the signs of the potential coupling matrix elements, Dagdigian et al.[41] showed that inelastic scattering of the intermediate case or Hund's case (b) molecule with a π^1 electron configuration, such as NO($^2\Pi$)

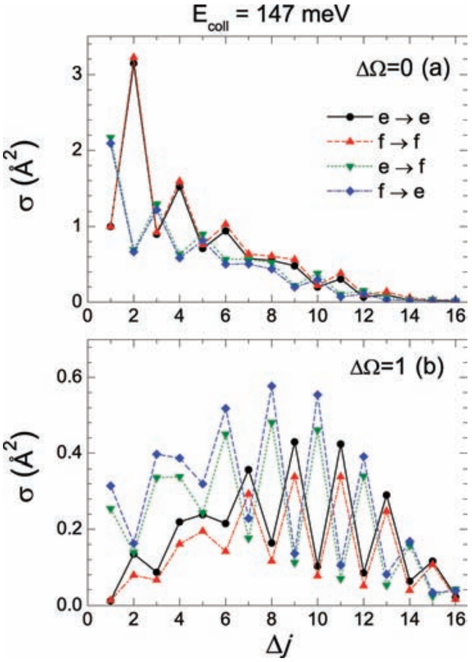

Figure 4. The o-s QM ICSs for e → e (black ●), f → f (red ▲), e → f (green ▼), and f → e (blue ♦) collisions out of the NO($^2\Pi_{1/2}, v = 0, j = 0.5$) level for (a) $F_1 \rightarrow F_1$ and (b) $F_1 \rightarrow F_2$ transitions at 147 meV.

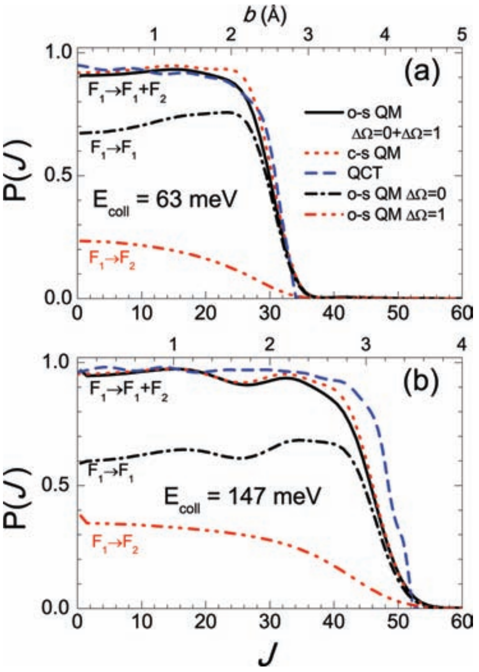

Figure 5. (a) Total opacity functions calculated using QCT (blue - - -), o-s QM (black —), and c-s QM (red — — —) methods for the He + NO(X) rotational excitation process out of the lowest rotational level at E_{coll} = (a) 63 and (b) 147 meV. The o-s QM opacity functions have been summed over the final and averaged over the initial Λ-doublet components and are also summed over the final spin−orbit states. The results from o-s QM calculations are also shown resolved into spin−orbit-conserving and spin−orbit-changing transitions. The upper *x*-axis shows the corresponding values of the impact parameter, *b*, from the QCT calculations.

and CH($^2\Pi$), preferentially populates the A″ (F_1f and F_2e) Λ-doublet levels, while for π^3 molecules, such as OH($^2\Pi$) or CN($^2\Pi$), the reverse behavior is expected (i.e., the A′ states F_1e and F_2f would be more populated). The present results are in agreement with these predictions, as previously found in the study by Yang and Alexander.[34]

The ICSs shown in Figure 4 for both spin−orbit-conserving and -changing collisions show oscillations with Δj, depending on whether the transitions conserve or change parity. The results at E_{coll} = 63 meV are similar to the ones at E_{coll} = 147 meV, although the oscillations are more pronounced in the latter case. As noted in section II.B.2., the oscillatory structure observed in the rotational level dependence of the ICSs arises from the dominance of even terms in the Legendre expansion of the intermolecular potential, eqs 5 and 6, which reflects the near-homonuclear character of the NO(X) molecule. A full account of these propensities has been given previously[5,6,34,50] and will not be repeated here. Note, however, that McCurdy and Miller have provided an alternative explanation for the oscillatory structure in terms of an interference effect originating from scattering from either ends of the molecule.[51] They also observed that the change in phase of the oscillatory structure with increasing Δj, evident in the data shown in Figure 4, could be associated with the relative magnitudes of even and odd terms in the expansion of the potential.[34,51]

B. Total Opacity Functions. Figure 5 shows a comparison between the o-s QM, c-s QM, and QCT total opacity functions for inelastic scattering (obtained by summing over all inelastic excitations) at E_{coll} = 63 and 147 meV. The QCT opacity functions are quite flat and near unity at low impact parameters, with the plateaus extending to somewhat larger impact parameters at the higher collision energy. They then fall sharply to 0 at around 2.5−3.0 Å. It is interesting to compare the He−NO(X) system with Ar−NO(X), for which a distinct secondary maximum was observed in the opacity functions at higher impact parameters, which was attributed to the attractive part of the intermolecular potential and to an "*L*-type" rainbow.[42] For the Ar−NO(X) system, the well depths on the A′ and A″ surfaces are 116 and 111 cm^{-1}, respectively,[52] while for He−NO(X), the well depths on the A′ and A″ PESs employed here are only 29 and 25 cm^{-1}, respectively[36] (see Figures 1 and 2). Because of these lower values, the attractive part of the He−NO(X) potential cannot cause significant rotational excitation at higher impact parameters, and therefore, the secondary maximum in the opacity function is extremely weak. One might expect that at lower collision energies, the attractive part of the potential would be more important, but it was found that the secondary peak remains very weak at E_{coll} = 33 meV.

The results of c-s QM quantum mechanical calculations for the He−NO(X) system are in very good agreement with the QCT studies, as also found for the Ar−NO(X) system.[42] The o-s QM opacity functions are similar to the QCT and c-s QM predictions, once the open-shell opacity functions for both $F_1 \rightarrow F_1$ and $F_1 \rightarrow F_2$ are summed. Notice, therefore, that the role of V_{diff} in this system is primarily to partition flux between the F_1 and F_2 manifolds. In the o-s QM calculations, the opacity functions for the spin−orbit-conserving transitions show significantly higher probabilities at higher impact parameters than the spin−orbit-changing transitions. This arises partly because the spin−orbit-conserving transitions are governed by V_{sum}, which, in general, is more attractive at long-range than V_{diff}. Note also, though, that the spin−orbit-changing transitions tend to be associated with higher rotational excitation than the spin−orbit-conserving transitions, and they tend to arise from lower impact parameter collisions.

Fully quantum state-to-quantum state-resolved opacity functions have also been calculated using both QCT and QM methods, and the o-s QM data were presented in our preliminary

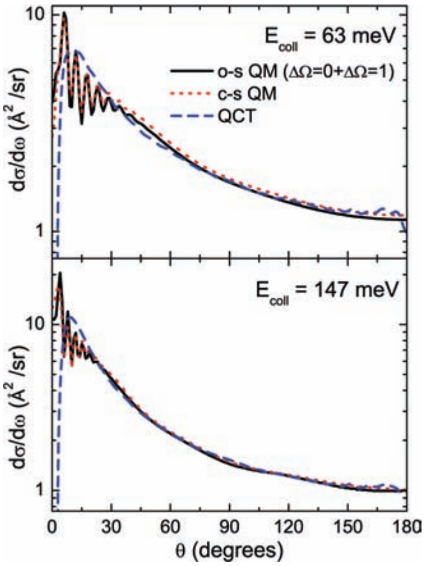

Figure 6. Total DCSs for inelastic excitations out of the lowest rotational level of NO($^2\Pi_{1/2}$,$v = 0$) summed over all final rotational transitions for $E_{\mathrm{coll}} = 63$ (upper panel) and 147 eV (lower panel) obtained from the o-s QM (black —), c-s QM (red • • •), and QCT (blue - - -) calculations. The o-s QM data have been summed over all spin−orbit transitions.

Communication of these results.[37] These state-resolved opacity functions will not be presented again here but will be discussed briefly in the context of the state-resolved DCSs presented in the following subsection.

C. Differential Cross Sections. ***1. Total Differential Cross Sections.*** The QCT, c-s QM, and o-s QM total DCSs exhibit a strong preference for forward scattering (see Figure 6). Both o-s QM and c-s QM show narrow glory-type diffraction oscillations at small scattering angles due to interferences of “trajectories” with large angular momenta that pass through the long-range part of the potential and emerge close to the forward direction. The angular separation of these diffraction peaks is constant over different scattering angles and final j' and is usually approximated by the equation[53]

$$\Delta\theta \approx \frac{\pi}{kR_{\mathrm{m}}} \tag{10}$$

where

$$k = \frac{\sqrt{2\mu E_{\mathrm{coll}}}}{\hbar} \tag{11}$$

is the initial wavenumber vector, μ is the reactant reduced mass, and R_{m} is the location of the minimum of the potential well. The diffraction peaks at $E_{\mathrm{coll}} = 63$ meV in Figure 6 are separated by ~5.7°, which yields a value of $R_{\mathrm{m}} \simeq 6$ a_0, quite close to the location of the minimum indicated in Figure 1. The angular range over which this diffraction is significant becomes larger as the potential well depth increases[54] and consequently is rather narrow for the He−NO(X) system. Employing a Fraunhofer model, a similar diffraction pattern was recently reported for the analogous system NO(X)−Ar.[55] The range also decreases as j' increases, in agreement with predictions by Schinke and co-workers for similar systems.[54] Owing to the fact that the diffraction patterns at low scattering angles are a manifestation of quantum mechanical behavior, the QCT calculations do not reproduce this oscillatory structure. They predict no inelastic scattering at $\theta = 0°$ (recall that the DCSs depicted in Figure 6 do not include elastic scattering) and since the lowest angles are classically forbidden for inelastic scattering, the QCT calculations yield much lower values for the DCS than the o-s QM and c-s QM predictions at θ between 0 and ~5°. For larger scattering angles, the QCT results are in very good agreement with the o-s and c-s QM calculations. At the higher collision energy (147 meV), the total DCS shows similar behavior but with slightly more forward scattering.

2. Spin−Orbit State-Resolved Differential Cross Sections. DCSs for inelastic scattering into individual final rotational levels at $E_{\mathrm{coll}} = 147$ meV, obtained from the o-s QM calculations and resolved into $F_1 \rightarrow F_1$ and $F_1 \rightarrow F_2$ transitions, are displayed in Figure 7, which includes a comparison of the theoretical results with the experimental data of Meyer et al. at 147 meV.[14] As with the ICSs, the experimental DCSs have been scaled to the o-s QM results. Since the initial Λ-doublet level was not selected in the experiment, once these levels were averaged over in the o-s QM calculations, there was good agreement with the experiments. Note that the calculations account equally well for the DCSs of both the spin−orbit-conserving and the spin−orbit-changing collisions. Due to the counterpropagating molecular beam geometry employed in the experiments of Meyer et al.,[14] they have a rather poor angular resolution in the forward and backward direction. It seems likely that remaining discrepancies between experiment and theory mainly reflect this poor resolution. It should be noted that DCSs obtained from previous o-s QM calculations using the same PES as that employed here are in much better agreement with the fully quantum-state-resolved DCSs derived from the crossed molecular beam measurements of Gijbertsen et al. at a collision energy of 63 meV.[23]

For small Δj values, the DCSs for spin−orbit-changing collisions shown in Figure 7 are somewhat more forward scattered than those for spin−orbit-conserving transitions. As Δj increases, the shapes of the DCSs (but not the magnitudes) become increasingly similar. These effects were also observed previously in the calculations by Yang and Alexander.[34] The differences in the DCSs at low Δj are somewhat surprising given the total opacity functions shown in Figure 5, which showed that spin−orbit-changing collisions have, on average, a preference for low J collisions, compared with the spin−orbit-conserving transitions. However, the product state-resolved opacity functions indicate that, for a given Δj, the spin−orbit-changing collisions, in fact, sample higher J values than the spin−orbit-conserving transitions. The difference in scattering for low rotational excitation probably reflects differences in V_{sum} and V_{diff} (see Figure 1) and the ranges of the specific expansion terms in the potentials, $V_{l0}(R)$ and $V_{l2}(R)$ shown in Figure 2, that are responsible for particular transitions. However, the specific cause remains unclear. Despite the difference between the V_{diff} and V_{sum} potentials, the DCSs for $F_1 \rightarrow F_1$ and $F_1 \rightarrow F_2$ transitions become very similar at higher final rotational levels. A possible explanation is that at higher rotational levels, the spin−orbit states become mixed, and therefore, the dynamics for these two different paths would become similar, as was observed with the ICSs.

The QCT and c-s QM DCSs for $\Delta j = 5-8$ transitions are represented in the top panel of Figure 8. At low scattering angles, the c-s QM results have significantly larger cross sections than the QCT calculations and show diffraction patterns for $\Delta j \leq 4$

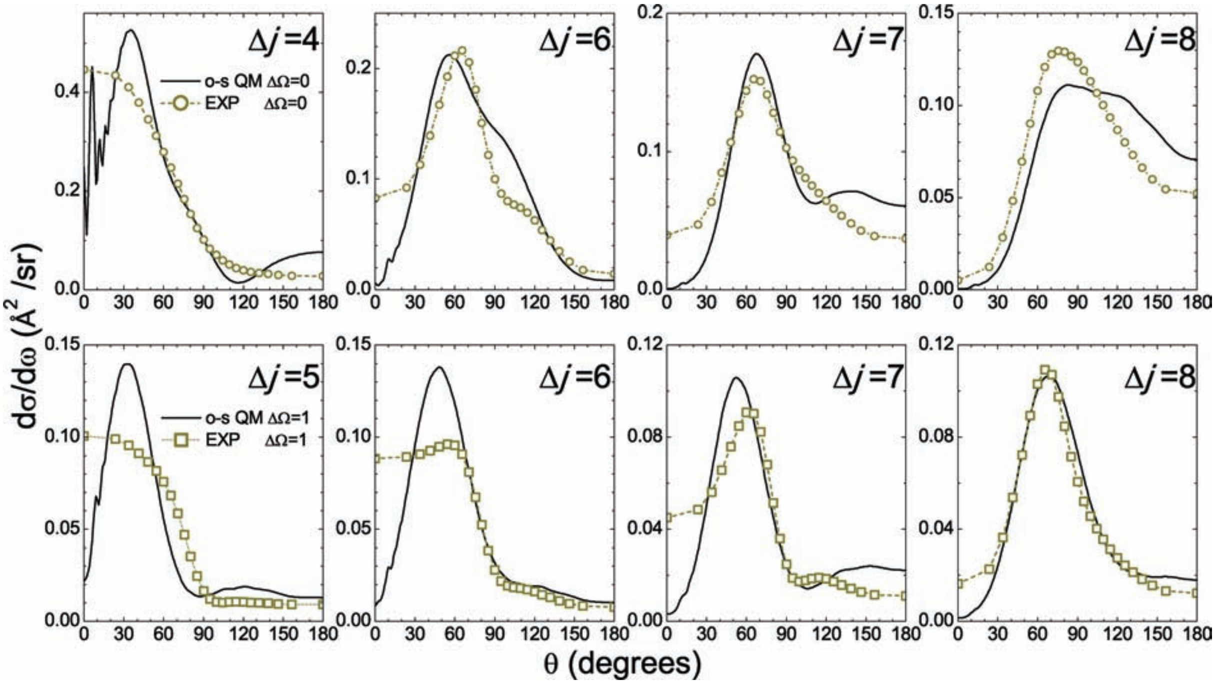

Figure 7. Upper panels: Comparison of the rotationally resolved DCSs for $F_1 \rightarrow F_1$ transitions at $E_{\text{coll}} = 147$ meV obtained from o-s QM (—) calculations averaged over the initial Λ-doublet levels with the experimental results obtained from ref 14, The experimental data have been scaled to the theoretical o-s QM results. Lower panels: As in the upper panels, but for $F_1 \rightarrow F_2$ collisions. The initial state is NO($^2\Pi_{1/2}, v = 0, j = 0.5$), and in each panel, the value of Δj is given.

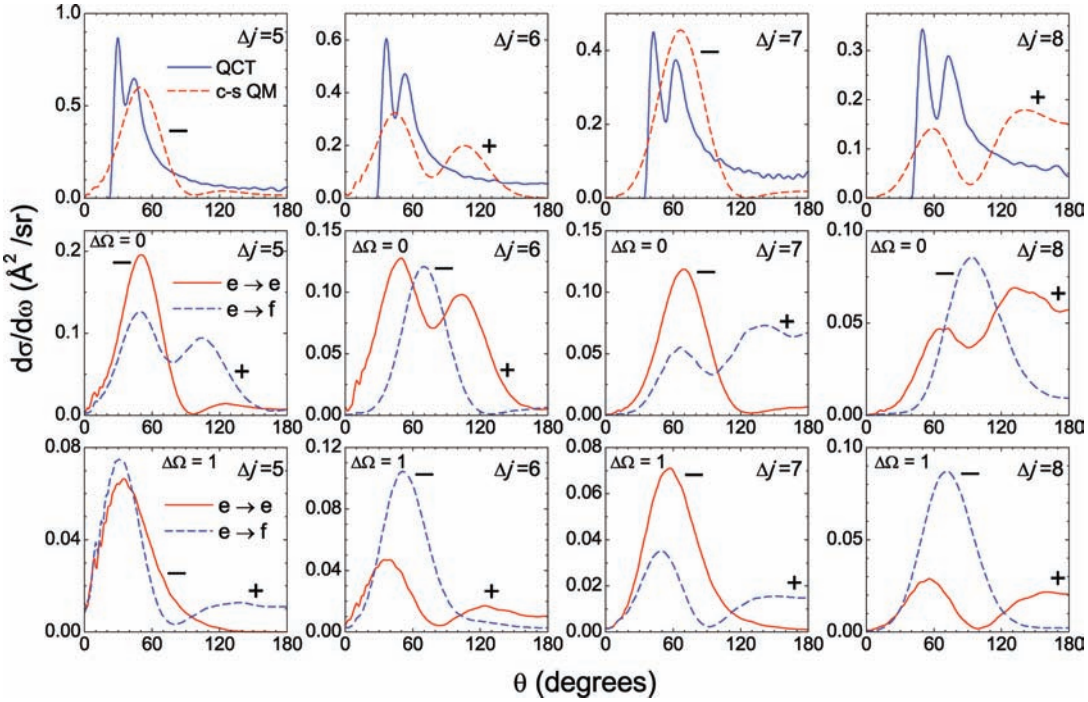

Figure 8. Top row: Comparison of DCSs obtained from the QCT and c-s QM calculations at $E_{\text{coll}} = 147$ meV starting from the lowest rotational state of NO(X) and showing transitions in the range from $\Delta j = 5$ to 8. Middle row: As for the top row but showing o-s QM full state-to-state DCSs for rotational excitation from the lowest rotational state of NO(X) in the F_1 spin−orbit manifold. Results are shown for e → e (red —) and e → f (blue − − −) transitions into the F_1 manifold at $E_{\text{coll}} = 147$ meV. Bottom row: As for the middle row but showing the o-s QM DCSs for transitions into the F_2 manifold. Total parity-conserving/changing transitions are denoted by + and −, respectively. Note the appearance of double peaks in the c-s QM and o-s QM calculations for parity-conserving transitions. See text for details.

transitions, as discussed above in the context of the total DCSs. The QCT DCSs are sharper and rise fairly abruptly from the low-angle side and then decline more slowly toward backward scattering angles. This behavior can be attributed to orientational rainbows in which the "dark" side of the rainbow corresponds to small angles and the "bright" side to larger angles. In the classical case, the low-angle region is forbidden, while in the QM case for $\Delta j > 4$, they die smoothly as $\theta \rightarrow 0$. Due to these interference phenomena, the agreement between QCT and c-s QM data is, in general terms, only qualitative.

Interestingly, the QCT DCSs exhibit a single peak at the lowest rotational levels, but at the higher Δj values shown in the figure, a double peak structure becomes apparent. The positions of both peaks move toward the backward direction, and their separation increases with increasing final rotational level. This double peak structure seems to be absent in the Λ-doublet averaged o-s QM data shown in Figure 7.

3. Effect of Parity on the Differential Cross Sections. The two lower panels of Figure 8 show the fully quantum-state-resolved o-s QM calculations. Only data for the initial $\Omega = 1/2$, $j = 1/2$, e Λ-doublet level are shown at 147 meV collision energy. Remarkably, a double peak structure now emerges in the o-s QM calculations, but only for transitions to certain rotational states. Two peaks are observed in the e → e transitions when Δj = even and in the e → f transitions when Δj = odd, irrespective of the final spin−orbit state. As noted in ref 37, in the o-s QM calculations, the double peaks appear in the Λ-doublet-resolved DCSs for total parity-conserving transitions (labeled in Figure 8 with a + sign). Similarly, in the c-s QM calculations, the double peak feature shows up only for parity-conserving transitions, which, in this case, correspond to even Δj transitions (see the upper panels of Figure 8). As might be expected, the shape, although not the magnitude, of the c-s DCS is remarkably similar to that obtained in the o-s QM calculations for the same total parity; compare, for instance, the c-s QM DCS for $\Delta j = 6$ and $\Delta j = 7$ with those resulting from o-s QM calculations for the $\Delta j = 6$ e → e, and $\Delta j = 7$ e → e transitions. The reason for the similarity in the DCSs is that both the c-s and o-s calculations for the same Δj and change in parity probe the same terms in the summed potential, V_{sum}. We return to the role of various expansion terms in the potential and of the potential coupling matrix elements later in the discussion. While the angular distributions from the QCT calculations show a double peak structure at both collision energies studied, the c-s and o-s QM DCSs only show a double peak structure at 147 meV. Furthermore, the positions of the peaks that belong to these Λ-doublet-resolved DCSs are different from the peak positions in the QCT case. Although the DCSs for spin−orbit-conserving and spin−orbit-changing collisions show some differences in detail, the pattern of single and double peaks for the two sets of data are quite similar, as discussed further below. Once the o-s QM DCSs are summed over the final and/or averaged over the initial Λ-doublet states, the two peaks are not clearly observed, as shown in Figure 7, at least at the present collision energy for the range of final rotational states depicted.

We have previously shown that the existence of double peaks in o-s QM DCSs for spin−orbit-conserving transitions at 147 meV are closely related to the existence of double peak structures in the corresponding partial cross sections and to specific expansion terms of the potential.[37] For the e → e (or f → f) transition with Δj = even, a shoulder appears in the opacity functions at 147 meV and thus a double peak in their corresponding partial cross sections. For e/f-changing collisions, a double peak appears for Δj = odd. Therefore, the double peak in the fully state-resolved o-s QM DCSs appears to be correlated with two different peaks in the corresponding partial cross sections. The DCSs giving rise to two maxima (those for the parity-conserving transitions) have been analyzed by adding successive partial waves with increasing J contributions in order to understand the buildup of the DCS. These maxima seem to be due to different ranges of J. In particular, for $\Delta j = 6$ in the c-s QM calculations, it was found that the most backward peak is caused by partial waves summed up to $J = 30$ and that addition of more partial waves does not substantially change the shape or the magnitude of this backward maximum, whereas for this range of J, the forward peak is absent. In turn, the forward peak only builds up with the addition of $J > 30$, and it is only fully converged with $J_{\max} = 50$. In the case of the QCT calculations, the buildup of the DCS is qualitatively similar, although not so well-defined; contributions of $J \leq 40$ are needed in order to get the backward maximum, but in this range of impact parameters, the forward peak is already partially formed. As was pointed out in ref 37, the state-resolved bimodal opacity function maps the shape of the DCS in the QM calculations; low J causes the backward peak, while the secondary peak in the $P(J;j \rightarrow j')$ is responsible for the forward maximum in the DCS.

As discussed in our preliminary Communication,[37] the double peak structure in the DCSs, and their appearance only for transitions that conserve total parity, can be attributed to specific expansion terms of the intermolecular potential and to the symmetry properties of the potential coupling matrix elements given in eq 8. Assuming that Hund's case (a) is a good approximation for the NO(X) rotational levels examined here, for the e initial Λ-doublet state, the potential coupling matrix elements of eq 8 contain the specific terms[5]

$$\sum_l [1 + \epsilon'(-1)^{\Delta j + l}] \begin{pmatrix} L' & l & L \\ 0 & 0 & 0 \end{pmatrix} \begin{pmatrix} j' & l & \frac{1}{2} \\ -\frac{1}{2} & 0 & \frac{1}{2} \end{pmatrix} \begin{Bmatrix} \frac{1}{2} & L & J \\ L' & j' & l \end{Bmatrix} V_{l0}(R) \tag{12}$$

and

$$\sum_l [1 + \epsilon'(-1)^{\Delta j + l}] \begin{pmatrix} L' & l & L \\ 0 & 0 & 0 \end{pmatrix} \begin{pmatrix} j' & l & \frac{1}{2} \\ -\frac{3}{2} & 2 & -\frac{1}{2} \end{pmatrix} \begin{Bmatrix} \frac{1}{2} & L & J \\ L' & j' & l \end{Bmatrix} V_{l2}(R) \tag{13}$$

for the spin−orbit-conserving and -changing collisions, respectively. In the weak coupling limit, the ICSs and DCSs would directly reflect the potential matrix elements,[6,34] and this is indeed found to be the case for low Δj transitions, which tend to sample the long-range part of the potential and involve large orbital angular momenta, L.[37] For higher Δj, which involve lower L values, inelastic scattering can be described approximately using an extended treatment, involving tiers of "virtual" states,[37] again connected by specific sets of terms in the potential. Parity-conserving transitions were shown to be coupled by pathways involving distinct potential terms compared with the total parity-changing collisions.[37] In particular, it was shown that a key feature of the parity-conserving transitions was that they could be coupled by purely odd terms in the potential, and it was these odd terms in the potential that were responsible for the double peaks in the DCSs.[37]

Comparison of eqs 12 and 13 shows that the potential matrix elements for spin−orbit-changing collisions are very similar to those for spin−orbit-conserving collisions. Note, in particular, that the symmetry factor $[1 + \epsilon'(-1)^{\Delta j + l}]$ for the e initial state is the same. Depending on the potential expansion terms $V_{l0}(R)$ and $V_{l2}(R)$, this would imply, within a direct scattering model,[37] that the DCSs for spin−orbit-conserving and -changing collisions should show similar patterns of behavior, something which is in agreement with the o-s QM calculations presented in Figure 8. Such similarities have been observed experimentally by Gijsbertsen et al.[23] for DCSs with $\Delta j > 3$ for He + NO collisions at E_{coll} of 63 meV and are also in agreement with predictions of the QQT treatment of Stolte and co-workers.[25,26,28] It was

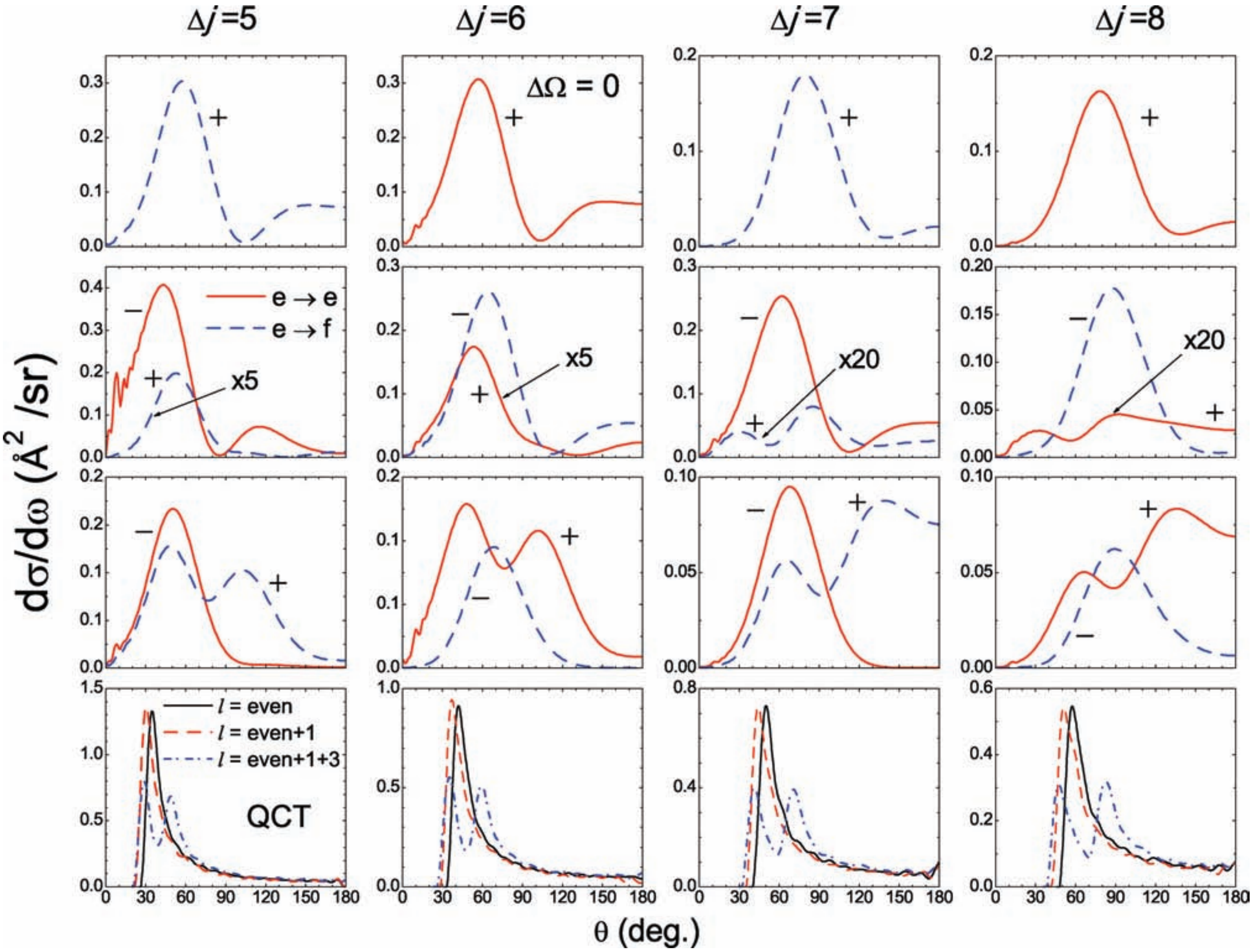

Figure 9. The o-s QM fully state-to-state resolved DCSs for rotational excitation from the lowest rotational state of NO to the F_1 spin−orbit manifold at 147 meV. Results are shown for parity-conserving (+) and parity-breaking (−) transitions obtained from calculations where only l = even (top row), l = even plus $l = 1$ (second row), and l = even plus $l = 1$ and 3 (third row) terms of the potential are included. The latter data are very similar to those obtained using the full potential (Figure 8). The parity-conserving transitions are e → e for Δj even and e → f for Δj odd. The bottom row shows the results of the QCT calculations in which different l terms in the expansion of the potential are retained. Note that, as with the o-s QM data, double peaks are only observed if the $l = 3$ term in the potential is included.

argued there that DCSs exhibit similar shapes for scattering into states of the same total parity, p, and a common value of $n = j' - \epsilon\epsilon'/2$. Although QQT has not yet been extended to spin−orbit-changing collisions, it is interesting to note that the parity, p, of any chosen j' rotational level in the F_1 and F_2 manifolds is the same, offering support to the above arguments for the similarity of DCSs across different spin−orbit manifolds.[56] The present calculations corroborate this finding, not only with regard the shape but also the magnitude of the DCSs.

The appearance of a double peak structure in c-s and o-s QM calculations only at 147 meV, and not at 63 meV, is intriguing. It might be taken to suggest that, because the He atom can approach much closer to the NO molecule at the higher collision energy, it therefore sees a stronger anisotropy in the PES. However, if that is the case, it is surprising that the anisotropy of the V_{sum} potential at the energies corresponding to the two values of E_{coll} shown in Figure 1a are so similar. Furthermore, double peaks are seen in the QCT calculations at both collision energies. This suggests that the mechanism responsible for production of the double peak structure in the QCT and QM calculations is different. An additional factor to consider in the QM case is the difference in de Broglie wavelengths at the two collision energies, which leads to a difference in phase shifts. The higher phase shift at the higher collision energy allows enhanced interference between tiers of virtual states. It is this interference, which is effectively an interference between scattering at either ends of the molecule, that is responsible for the double peaks in the QM differential cross sections.[26,37,56]

4. The Role of V_{10} and V_{30} Expansion Terms and the Classical Dynamics. The role of various even and odd terms in the potential has also been examined in ref 37. As shown in Figure 9 for the spin−orbit-conserving transitions, when only even potential terms, $V_{l0}(R)$, are included in the o-s QM calculations, the cross sections for total parity-nonconserving transitions vanish, and the double peak structure in the DCSs for the parity-conserving transitions disappears.[37] Furthermore, calculations in which only l = even plus $l = 1$ terms in the potential are included are sufficient to reproduce the shape of the DCS for the total parity-changing collisions (labeled with a − sign), as shown in the second row of Figure 9, but not for the parity-conserving collisions. The third row of Figure 9 demonstrates that it is the $l = 3$ term in the potential that is required in the o-s QM calculations to reproduce the double peak structure in DCSs for parity-conserving transitions. The final row in the figure allows comparison of these o-s QM results with the QCT DCSs obtained for the same set of Δj transitions, including different expansion terms in the potential. Inclusion

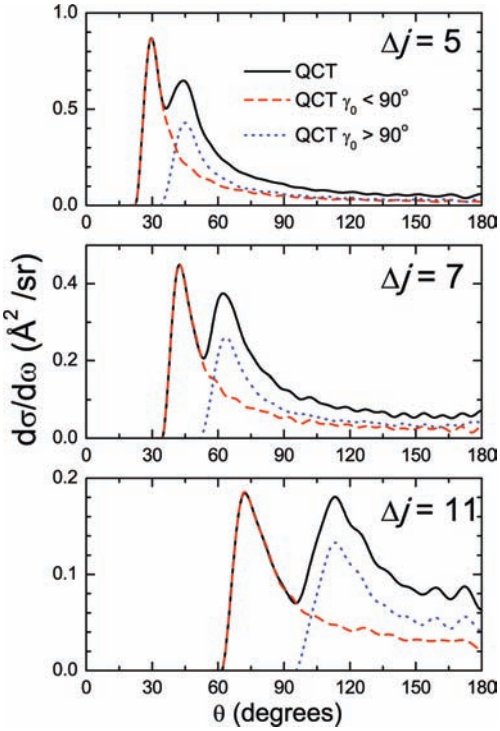

Figure 10. QCT (black —) state-resolved inelastic DCSs for rotational excitation from the lowest rotational state of NO into $j' = 5$ (top panel), 7 (middle panel), and 11 (bottom panel). DCSs for those trajectories which have Jacobi angles at the distance of closest approach, γ_0, less than 90° (red — — —) or larger than 90° (blue - - -) are presented for comparison. Notice that the classical double peak rotational rainbow in the QCT DCS clearly results from the potential anisotropy; the first peak proceeds from trajectories probing the N-side of NO, whereas the second is due to those attacking the O-side. If the potential were symmetric, the two peaks would coalesce into a single peak centered between the observed peaks (see Figure 9).

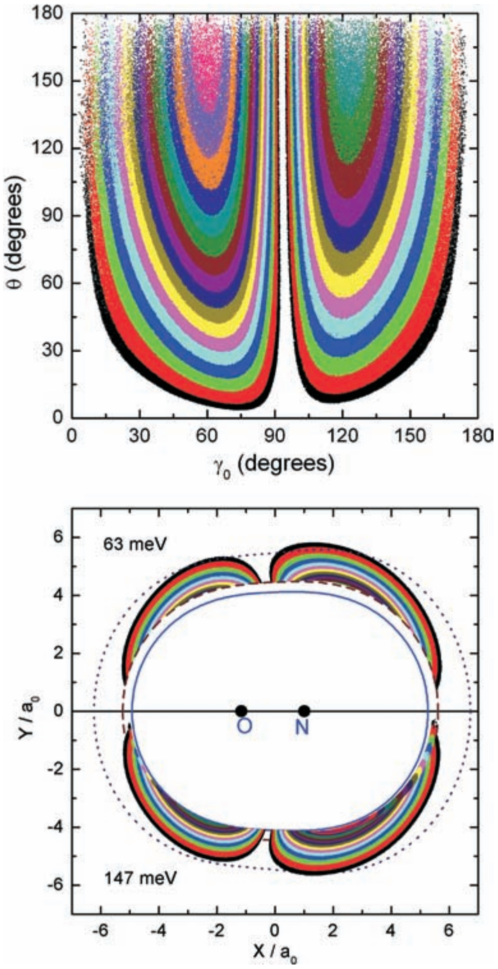

Figure 11. Top panel: Scattering angle versus angle of closest approach, γ_0, for trajectories leading to specific Δj rotational transitions. Layers denote different final Δj, starting with $\Delta j = 1$ for the outermost layer. Notice the asymmetry about the node at ~95°. Bottom panel: A plot of the location of the closest approach in Cartesian coordinates of the body-fixed frame (see text for details) for trajectories leading to specific Δj rotational transitions. The O-side ($\gamma = 180°$) of the molecule is as that in Figure 1, and the layers are as those in the top panel. The upper half of the bottom panel is for $E_{\mathrm{coll}} = 63$ meV, and the bottom half is for $E_{\mathrm{coll}} = 147$ meV. Dotted, dashed, and solid (blue) lines represent the contours at 0, 63, and 147 meV, respectively, of the V_{sum} potential. In the regions of T-shaped and collinear approach, there are no trajectories leading to rotational excitation. The shape of the trajectory layers exhibits a clear asymmetry due to the anisotropy of the potential.

of l = even plus the first odd term, $l = 1$, in the expansion of the potential makes the DCSs only slightly more forward compared with running trajectories on a PES with only l = even terms present. Furthermore, as with the o-s QM data, it is not until the $l = 3$ expansion term is included in the PES that the double peak structure in the QCT DCSs is recovered. Although the shape and detailed mechanism of production of the double peaks observed in the QCT and o-s QM DCSs are different, the fact that the structures arise from the same term in the expansion of the PES indicates that both phenomena are related to the anisotropy of the potential.

The distinctive structure of the QCT DCSs, which is usually described in terms of rotational rainbows or orientation interference structures, has been extensively studied in the past (see, for example, refs 57−59). The origin of the double peaks in the QCT calculations is due to the different shape of the potential at $\gamma < 90°$ compared with that at $\gamma > 90°$. Upon repeating the QCT calculations with a symmetrized PES (i.e., forcing the potential to look like that of a homonuclear diatomic molecule by setting the odd terms in the potential to 0), the double peak structure disappears, and only one peak, situated in the center of the former double peak, emerges (see the bottom panels of Figure 9). Figure 10 illustrates the effect of selecting the trajectories according to whether the Jacobi angle at the distance of closest approach, γ_0, is either less than or greater than 90°. Trajectories for which $\gamma_0 < 90°$ give rise to a single peak in the DCS at the location of the more forward of the double peaks, while trajectories with $\gamma_0 > 90°$ give rise to the more backward of the two peaks. Recall that $\gamma_0 < 90°$ corresponds to He attacking the N-end of NO. If one uses a simple ball-and-stick model[22] for the NO molecule, where N is the stick and the heavier O atom is the ball, it is easier to rotate NO by hitting the stick than the ball. This is clear in Figure 10, where it is seen that the DCSs for collisions with $\gamma_0 < 90°$ occur at smaller scattering angles than those in which $\gamma_0 > 90°$.

This effect is more clearly seen in the plots of Figure 11. In the top panel of the figure, the scattering angle of each trajectory is represented as a function of its angle of closest approach, γ_0, for different Δj transitions (color coded). Notice that the there is node close to 95° that corresponds to the location of the global minimum on the V_{sum} PES and, consequently, to the flatter contours of the repulsive potential (see Figure 1a). If the He atom hits that region, no rotational excitation takes place. The interesting feature is that the plot is not symmetric about the node region. For a given Δj (color) transition, the scattering angles corresponding to $\gamma_0 < 95°$ are on average smaller than those for the $\gamma_0 > 95°$. Moreover, as Δj increases, the mismatch between the scattering angles to the left and right of the node region become more pronounced.

In the bottom panel of Figure 11, the distances and angles of closest approach are plotted for different Δj transitions (color coded) starting with $\Delta j = 1$ as the outermost layer. The figure demonstrates that collisions with γ_0 at around 60 and 120° are the most efficient in promoting rotational excitation, partly reflecting kinematic factors as well as the increased anisotropy of V_{sum} at these angles. Note that at the higher collision energy (shown in the bottom half of the figure), the trajectories probe more the anisotropic repulsive part of the potential that is responsible for the double peak structure in the DCSs. Figure 11 also illustrates the reason that collisions into high rotational levels have smaller cross sections. These collisions have to access a rather restricted range of γ_0 values compared to collisions that result in low rotational levels.

The roles of the different terms in the expansion of $V_{\text{sum}}(\gamma,R)$ are actually rather subtle, as illustrated in Figure 12. With only even l terms included in the potential, it becomes symmetrical and equivalent to that of a homonuclear diatomic (top panel). Inclusion of the $V_{10}(R)$ expansion term, the dominant odd term in the expansion (see Figure 2), leads to a highly asymmetric potential (middle panel). Remarkably, however, both the QCT and o-s QM calculations run with this potential give rise to DCSs with just a single peak, slightly shifted toward forward scattering angles; see the bottom panels of Figure 9. The potential appears to be "too heteronuclear" in character to generate a double peak. In fact, attack at the two sides of the molecule with this potential generates peaks at very similar scattering angles. What seems to occur is that the asymmetry of the PES compensates for the effects of kinematics. Addition of the V_{30} term (bottom panel) actually make the potential more symmetrical in nature, as is required to generate double peaks in the DCSs. Notice that the potential which includes even terms, plus the first two odd terms, V_{10} and V_{30}, is sufficient to recover closely the full PES (see Figure 1a).

5. Comparison with Other Systems. Although two peaks have been observed in the energy loss spectra at fixed scattering angle for K + CO, Xe + CO_2, and D_2 + CO,[59−64] Houston and co-workers were probably the first to directly observe a clear double peak in the DCS following inelastic scattering. Double peaks were observed for NO($^2\Pi_{1/2}$,$j' = 18.5$) generated via inelastic scattering between Ar and NO molecules at 180 meV[65] but were not observed at 110 meV and were only just visible at 390 meV. Jons et al., studying the same system, found evidence of two maxima for NO($^2\Pi_{1/2}$,$j' = 14.5$) at a collision energy of 54.8 meV, and two maxima were also clearly seen for NO($^2\Pi_{1/2}$,$j' = 18.5$) at a collision energy of 210.3 meV.[66] Houston and co-workers also observed a hint of a double peak structure in the DCS for the most highly rotationally excited products of rotationally inelastic scattering of NO($^2\Pi_{1/2}$,$v = 5$) by Ar at 181.1 meV.[67] In contrast, QCT calculations suggest that only one peak is observed in the He−CO system. The PES for the latter system[68] is noticeably more symmetric than that for He−NO(X). However, multiple peaks in the DCSs have been observed for Ne−CO.[28,69,70] It is evident that a clear manifestation of double peaks in the DCS is very sensitive to the collision energy, initial spin−orbit and vibrational state, and final NO rotational level.

The appearance of double peaks only for specific Λ-doublet levels has not yet been observed experimentally. However, it is a common feature of a number of systems involving scattering of NO(X) by the rare gases. For example, double peak structure appears in both o-s and c-s calculations in Ne−NO(X) (work in progress) and Ar−NO(X) systems but are not observed for Kr−NO(X) and Xe−NO(X) under similar collision energy conditions. Scattering experiments on these systems, at the fully quantum-state-resolved level, are likely to provide very detailed information about the potentials for these systems and on their inelastic scattering dynamics.

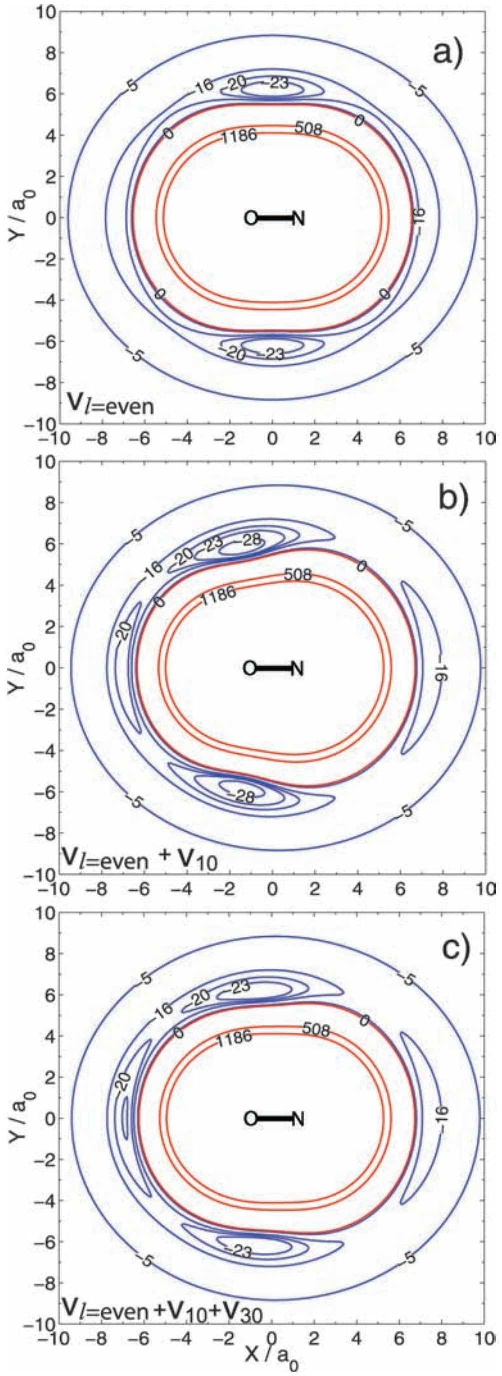

Figure 12. Contour plots of the summed potential $V_{\text{sum}}(\gamma,R)$ with only even l expansion terms included in the series in eq 5 (top panel), l even plus $l = 1$ (middle panel), and l even plus $l = 1$ and 3 (bottom left panel). The latter is almost identical to the full potential (see Figure 1).

IV. Summary and Conclusions

In this paper, a detailed QCT and QM study of inelastic scattering of NO(X) by He on the latest and most accurate

He−NO(X) PES[36] has been reported. Opacity functions and state-resolved ICSs and DCSs have been presented at collision energies of 63 and 147 meV. The calculated ICSs have been compared with two sets of experiments performed by Joswig et al.[13] at 63 meV and by Meyer[14] at 147 meV and with calculations by Yang and Alexander on a previous CEPA PES.[34] Overall, the agreement between experiment and theory is very good. Experimental DCSs obtained by Meyer have been compared with the theoretical calculations from this work and also show satisfactory agreement. Rotational rainbows are observed in some of the DCSs, and they move to higher scattering angles with the increasing NO final rotational level. Confirming and extending the findings at the lower collision energy of 63 meV by Gijsbertsen et al.,[23,26] the $F_1 \rightarrow F_2$ transitions are predicted to yield more forward scattered products than $F_1 \rightarrow F_1$ transitions also at 147 meV.

When the o-s QM DCSs are averaged over initial and summed over final Λ-doublet states, the DCSs obtained in this work appear as a single peak. Note that most of the experiments on the He−NO(X), in common with other systems, have not resolved the initial Λ-doublet state, and the results are consequently an average over these two levels. By contrast, the QCT results show a double peak structure at both collision energies, suggesting a significant disagreement between the classical and quantum calculations. However, once the DCSs from the o-s QM calculations are fully quantum-state-resolved, they too show a double peak structure, but only in the total parity-conserving transitions and only at the higher of the two collision energies studied. Similar behavior is also found in the c-s QM results, where the double peak structure is only observed for the even Δj (total parity-conserving) transitions. The structure in both the QCT and QM calculations has been shown to arise from a single specific expansion term in the potential, $V_{30}(R)$. Although the QCT method does not reproduce accurately all of the experimental and o-s QM results, it remains an indispensable theoretical tool to provide direct insight about the role that subtle details of the PES can play.

Acknowledgment. We would like to thank Henning Meyer for sending us the differential cross section data points and for useful discussions. The support of the U.K. Royal Society and EPSRC (via Programme Grant No. EP/G00224X/1) for grants to M.B. are gratefully acknowledged. S.M. acknowledges support of the SSF, CNRS, the British Council, and The Netherlands Organization for Scientific Research (NWO) for a research visit grant (PPS 883) and Dr. C. Vallance for many useful comments. J.K. acknowledges the financial support of the University Complutense of Madrid/Grupo Santander under the programme of Movilidad de Investigadores Extranjeros. This work has been funded by the Ministry of Science and Innovation of Spain under Grant CTQ2008-02578/BQU.

References and Notes

(1) Secrest, D. In *Atom−Molecule Collision Theory: A Guide for the Experimentalist*; Bernstein, R., Ed.; Plenum: New York, 1979.

(2) Levine, R. D.; Bernstein, R. B. *Molecular Reaction Dynamics and Chemical Reactivity*; Oxford University Press: Oxford, U.K., 1987.

(3) Lorenz, K. T.; Chandler, D. W.; Barr, J. W.; Chen, W.; Barnes, G. L.; Cline, J. I. *Science* **2001**, *293*, 2063.

(4) Kohguchi, H.; Suzuki, T.; Alexander, M. H. *Science* **2001**, *294*, 832.

(5) Alexander, M. H. *J. Chem. Phys.* **1982**, *76*, 5974.

(6) Degli-Esposti, A.; Berning, A.; Werner, H.-J. *J. Chem. Phys.* **1995**, *103*, 2067.

(7) Yang, X.; Dagdigian, P. J. *Chem. Phys. Lett.* **1998**, *297*, 506.

(8) Nizamov, B.; Dagdigian, P. J.; Alexander, M. H. *J. Chem. Phys.* **2001**, *115*, 8393.

(9) de Lange, M. J. L.; Stolte, S.; Taatjes, C. A.; Kłos, J.; Groenenboom, G. C.; van der Avoird, A. *J. Chem. Phys.* **2004**, *121*, 11691.

(10) Alexander, M. H.; Andresen, P.; Bacis, R.; Bersohn, R.; Comes, F. J.; Dagdigian, P. J.; Dixon, R. N.; Field, R. W.; Flynn, G. W.; Gericke, K.-H.; Grant, E. R.; Howard, B. J.; Huber, J. R.; King, D. S.; Kinsey, J. L.; Kleinermanns, K.; Kuchitsu, K.; Luntz, A.; McCaffery, A. J.; Pouilly, B.; Reisler, H.; Rosenwacks, S.; Rothe, E. W.; Shapiro, M.; Simons, J. P.; Vasudev, R.; Wiesenfeld, J. R.; Wittig, C.; Zare, R. N. *J. Chem. Phys.* **1988**, *89*, 1749.

(11) Keil, M.; Slankas, J. T.; Kuppermann, A. *J. Chem. Phys.* **1979**, *70*, 541.

(12) Beneventi, L.; Casavecchia, P.; Volpi, G. G. *J. Chem. Phys.* **1986**, *85*, 7011.

(13) Joswig, H.; Andresen, P.; Schinke, R. *J. Chem. Phys.* **1986**, *85*, 1904.

(14) Meyer, H. *J. Chem. Phys.* **1995**, *102*, 3151.

(15) Drabbels, M.; Wodtke, A. M.; Yang, M.; Alexander, M. H. *J. Phys. Chem. A* **1997**, *101*, 6463.

(16) Westley, M. S.; Lorenz, K. T.; Chandler, D. W.; Houston, P. L. *J. Chem. Phys.* **2001**, *114*, 2669.

(17) Barrass, P. A.; Sharkey, P.; Smith, I. W. M. *Phys. Chem. Chem. Phys.* **2003**, *5*, 1400.

(18) Sudbø, A. S.; Loy, M. M. T. *J. Chem. Phys.* **1982**, *76*, 3646.

(19) Imajo, T.; Shibuya, K.; Obi, K. *Chem. Phys. Lett.* **1987**, *137*, 139.

(20) James, P.; Sims, I. R.; Smith, I. W. M.; Alexander, M. H.; Yang, M. *J. Chem. Phys.* **1998**, *109*, 3882.

(21) Islam, M.; Smith, I. W. M.; Alexander, M. H. *Phys. Chem. Chem. Phys.* **2000**, *2*, 473.

(22) Gijsbertsen, A.; Linnartz, H.; Kłos, J.; Stolte, S. *Phys. Scr.* **2005**, *72*, C1.

(23) Gijsbertsen, A.; Linnartz, H.; Rus, G.; Wiskerke, A. E.; Stolte, S.; Chandler, D. W.; Kłos, J. *J. Chem. Phys.* **2005**, *123*, 224305.

(24) Gijsbertsen, A.; Linnartz, H.; Stolte, S. *J. Chem. Phys.* **2006**, *125*, 133112.

(25) Gijsbertsen, A.; Linnartz, H.; Taatjes, C. A.; Stolte, S. *J. Am. Chem. Soc.* **2006**, *128*, 8777.

(26) Ballast, A.; Gijsbertsen, A.; Linnartz, H.; Taatjes, C. A.; Stolte, S. A Quasi-Quantum Treatment of Inelastic Molecular Collisions. In *Proceedings of 25th International Symposium on Rarefied Gas Dynamics*; Ivanov, M. S., Rebrov, A. K., Eds.; Publishing house of the Siberian branch of the Russian Academy of Sciences: St. Petersburg, Russia, 2007; p 1263.

(27) Taatjes, C. A.; Gijsbertsen, A.; de Lange, M. J. L.; Stolte, S. *J. Phys. Chem. A* **2007**, *111*, 7631.

(28) Ballast, A.; Gijsbertsen, A.; Linnartz, H.; Stolte, S. *Mol. Phys.* **2008**, *106*, 315.

(29) Corey, G. C.; Alexander, M. H. *J. Chem. Phys.* **1986**, *85*, 5652.

(30) Nielson, G. C.; Parker, G. A.; Pack, R. T. *J. Chem. Phys.* **1977**, *66*, 1396.

(31) Manolopoulos, D. E. *J. Chem. Phys.* **1986**, *85*, 6425.

(32) Alexander, M. H.; Manolopoulos, D. E. *J. Chem. Phys.* **1987**, *86*, 2044.

(33) *HIBRIDON*, a package of programs for the time-independent quantum treatment of inelastic collisions and photodissociation; written by Alexander, M. H.; Manolopoulos, D. E.; Werner, H.-J.; Follmeg, B. with contributions by Vohralik, P. F.; Lemoine, D.; Corey, G.; Johnson, B.; Orlikowski, T.; Berning, A.; Degli-Esposti, A.; Rist, C.; Dagdigian, P.; Pouilly, B.; van der Sanden, G.; Yang, M.; de Weerd, F.; Gregurick, S.; Kłos. J.

(34) Yang, M.; Alexander, M. H. *J. Chem. Phys.* **1995**, *103*, 6973.

(35) Alexander, M. H. *Faraday Discuss.* **1999**, *113*, 437.

(36) Kłos, J.; Chałasiński, G.; Berry, M. T.; Bukowski, R.; Cybulski, S. *J. Chem. Phys.* **2000**, *112*, 2195.

(37) Kłos, J.; Aoiz, F. J.; Verdasco, J. E.; Brouard, M.; Marinakis, S.; Stolte, S. *J. Chem. Phys.* **2007**, *127*, 031102.

(38) Kłos, J.; Lique, F.; Alexander, M. H. *Chem. Phys. Lett.* **2008**, *455*, 1.

(39) Lique, F.; van der Tak, F. F. S.; Kłos, J.; Bulthuis, J.; Alexander, M. H. *Astron. Astrophys.* **2009**, *493*, 557.

(40) Huber, K. P.; Herzberg, G. *Constants of Diatomic Molecules*; Van Nostrand Reinhold: New York, 1979.

(41) Dagdigian, P. J.; Alexander, M. H.; Liu, K. P. *J. Chem. Phys.* **1989**, *91*, 839.

(42) Aoiz, F. J.; Verdasco, J. E.; Herrero, V. J.; Sáez Rábanos, V.; Alexander, M. H. *J. Chem. Phys.* **2003**, *119*, 5860.

(43) Aoiz, F. J.; Herrero, V. J.; Sáez Rábanos, V. *J. Chem. Phys.* **1991**, *94*, 7991.

(44) Aoiz, F. J.; Herrero, V. J.; Sáez Rábanos, V. *J. Chem. Phys.* **1992**, *97*, 7423.

(45) Arthurs, A. M.; Dalgarno, A. *Proc. R. Soc. London, Ser. A* **1960**, *256*, 540.

(46) Manolopoulos, D. E. *Close-Coupled Equations: The Log Derivative Approach to Inelastic Scattering, Bound State, and Photofragmentation Problems* PhD Thesis, Darwin College, University of Cambridge, United Kingdom, 1988.

(47) Hutson J. M.; Green, S. *MOLSCAT computer code*, version 14; Collaborative Computational Project No. 6 of the Engineering and Physical Sciences Research Council: United Kingdom, 1994.

(48) Orlikowski, T.; Alexander, M. H. *J. Chem. Phys.* **1983**, *79*, 6006.

(49) Zare, R. N. *Angular momentum: Understanding spatial aspects in Chemistry and Physics*; Wiley: New York, 1988.

(50) Alexander, M. H. *Chem. Phys.* **1983**, *92*, 337.

(51) McCurdy, C. W.; Miller, W. H. *J. Chem. Phys.* **1977**, *67*, 463.

(52) Alexander, M. H. *J. Chem. Phys.* **1999**, *111*, 7426.

(53) Schinke, R. *Chem. Phys.* **1978**, *34*, 65.

(54) Schinke, R.; Korsch, H. J.; Poppe, D. *J. Chem. Phys.* **1982**, *77*, 6005.

(55) Lemeshko, M.; Friedrich, B. *J. Chem. Phys.* **2008**, *129*, 024301.

(56) Ballast, A.; Stolte, S. **2009**, in preparation.

(57) Thomas, L. D. *J. Chem. Phys.* **1977**, *67*, 5224.

(58) Bosanac, S. *Phys. Rev. A* **1980**, *22*, 2617.

(59) Bosanac, S.; Buck, U. *Chem. Phys. Lett.* **1981**, *81*, 315.

(60) Beck, D.; Ross, U.; Schepper, W. *Z. Phys. A* **1979**, *293*, 107.

(61) Beck, D.; Ross, U.; Schepper, W. *Phys. Rev. A* **1979**, *19*, 2173.

(62) Andres, J.; Buck, U.; Meyer, H.; Launay, J. M. *J. Chem. Phys.* **1982**, *76*, 1417.

(63) Beck, D. In *12th International Conference: Phys. Electron. At. Collisions*; Datz, S., Ed.; North-Holland: Amsterdam, The Netherlands, 1982.

(64) Buck, U.; Huisken, F.; Otten, D.; Schinke, R. *Chem. Phys. Lett.* **1983**, *101*, 126.

(65) Bontuyan, L. S.; Suits, A. G.; Houston, P. L.; Whitaker, B. J. *J. Phys. Chem.* **1993**, *97*, 6342.

(66) Jons, S. D.; Shirley, J. E.; Vonk, M. T.; Giese, C. F.; Gentry, W. R. *J. Chem. Phys.* **1996**, *105*, 5397.

(67) Dixit, A. A.; Pisano, P. J.; Houston, P. L. *J. Phys. Chem. A* **2001**, *105*, 11165.

(68) Heijmen, T. G. A.; Moszynski, R.; Wormer, P. E. S.; van der Avoird, A. *J. Chem. Phys.* **1997**, *107*, 9921.

(69) McBane, G. C.; Cybulski, S. M. *J. Chem. Phys.* **1999**, *110*, 11734.

(70) Lorenz, K. T.; Chandler, D. W.; McBane, G. C. *J. Phys. Chem. A* **2002**, *106*, 1144.

JP9043732